nature chemistry

ARTICLES

https://doi.org/10.1038/s41557-018-0092-x

Dopant-induced electron localization drives CO_2 reduction to C_2 hydrocarbons

Yansong Zhou[1,2,10], Fanglin Che[1,10], Min Liu[1,3,4,10], Chengqin Zou[1], Zhiqin Liang[1], Phil De Luna[5], Haifeng Yuan[1,6], Jun Li[1,7], Zhiqiang Wang[8], Haipeng Xie[3], Hongmei Li[3], Peining Chen[1], Eva Bladt[9], Rafael Quintero-Bermudez[1], Tsun-Kong Sham[8], Sara Bals[9], Johan Hofkens[6], David Sinton[7], Gang Chen[2*] and Edward H. Sargent[1*]

The electrochemical reduction of CO_2 to multi-carbon products has attracted much attention because it provides an avenue to the synthesis of value-added carbon-based fuels and feedstocks using renewable electricity. Unfortunately, the efficiency of CO_2 conversion to C_2 products remains below that necessary for its implementation at scale. Modifying the local electronic structure of copper with positive valence sites has been predicted to boost conversion to C_2 products. Here, we use boron to tune the ratio of $Cu^{\delta+}$ to Cu^0 active sites and improve both stability and C_2-product generation. Simulations show that the ability to tune the average oxidation state of copper enables control over CO adsorption and dimerization, and makes it possible to implement a preference for the electrosynthesis of C_2 products. We report experimentally a C_2 Faradaic efficiency of 79 ± 2% on boron-doped copper catalysts and further show that boron doping leads to catalysts that are stable for in excess of ~40 hours while electrochemically reducing CO_2 to multi-carbon hydrocarbons.

Among CO_2 reduction products, C_2 hydrocarbons including ethylene (C_2H_4) and ethanol (C_2H_5OH) benefit from impressive energy densities and thus higher economic value per unit mass compared with C_1 counterparts[1–3]. To date, copper is one of the most promising candidates for electroreducing CO_2 to multi-carbon hydrocarbons. Previous research has shown that judiciously modified copper is especially selective for C_2 electroproduction[4–6]; however, C_1 and C_3 species are generated simultaneously[4,7]. It is of interest to modify copper to narrow the distribution of the products of the electrochemical reduction of carbon dioxide (CO_2RR) ultimately towards a single class of target hydrocarbons, and achieving such high selectivity combined with high activity is an important frontier for the field.

Surface $Cu^{\delta+}$ sites in copper catalysts have been suggested to be active sites for CO_2RR[8–10]: indeed, high Faradaic efficiencies for C_2 products have been achieved by introducing $Cu^{\delta+}$ into copper catalysts[11–13]. $Cu^{\delta+}$ has previously been introduced using oxygen-contained species, such as by deriving copper catalysts from oxidized copper[14–17]. However, the resultant $Cu^{\delta+}$ species are prone to being reduced to Cu^0 under CO_2RR, especially given the high applied reducing potentials needed to electrosynthesize C_2 compounds[18]. This has made the study of the role of $Cu^{\delta+}$ challenging and, at an applied level, it probably contributes to the loss in CO_2RR to multi-carbon performance over the first few hours of reaction[19,20].

We therefore took the view that introducing modifier elements—atoms that could tune and increase the stability of $Cu^{\delta+}$ in a lasting fashion, even following protracted CO_2RR—would contribute to the understanding of CO_2 reduction to C_2, as well as its practical implementation.

Results and discussion

Density functional theory (DFT) studies establish boron doping as a promising and stable candidate to modify copper in light of its adsorption behaviour on the Cu(111) surface (Fig. 1 and Supplementary Fig. 1). By a margin of 0.78 eV, it is more favourable for boron to diffuse into the subsurface of a Cu(111) slab than for it to remain on the surface (Fig. 1a)[21]. In addition to studying the boron-modified Cu(111) surface, we also examined computationally the boron-doped Cu(100) surface (see Supplementary Information)—the more thermodynamically favourable surface for producing C_2 products during CO_2RR. The results show that the subsurface sites are more favourable than the top or bridge adsorption sites. In contrast, oxygen is—by a margin of 1.5 eV—adsorbed on the Cu(111) surface rather than diffusing into the subsurface[22]. Together, these findings suggest that boron doping could offer a strategy for stable modulation of the copper catalyst.

We queried the projected density of states (PDOS) of Cu_{3d} and C_{2p} and carried out Bader charge analysis to investigate the electronic properties of boron-doped copper. When boron is doped into the subsurface of the copper slab, it exhibits a higher overlap among the binding states between C_{2p} and Cu_{3d} when CO adsorbs on the surface (Supplementary Figs. 4 and 5) compared with pristine copper, leading to a stronger binding energy of CO over a boron-doped copper surface. The d-band centre of the nearby copper atom shifts away from the Fermi level compared with pristine copper. This indicates that copper atoms adjacent to boron are more positively charged (Fig. 1a). The PDOS result agrees with Bader charge analysis: copper transfers electrons to boron, resulting in a positively

[1]Department of Electrical and Computer Engineering, University of Toronto, Toronto, Ontario, Canada. [2]MIIT Key Laboratory of Critical Materials Technology for New Energy Conversion and Storage, School of Chemistry and Chemical Engineering, Harbin Institute of Technology, Harbin, China. [3]Institute of Super-Microstructure and Ultrafast Process in Advanced Materials, School of Physics and Electronics, Central South University, Changsha, China. [4]State Key Laboratory of Power Metallurgy, Central South University, Changsha, China. [5]Department of Materials Science and Engineering, University of Toronto, Toronto, Ontario, Canada. [6]Department of Chemistry, KU Leuven, Leuven, Belgium. [7]Department of Mechanical and Industrial Engineering, University of Toronto, Toronto, Ontario, Canada. [8]Department of Chemistry, University of Western Ontario, London, Ontario, Canada. [9]EMAT, University of Antwerp, Antwerp, Belgium. [10]These authors contributed equally: Yansong Zhou, Fanglin Che, Min Liu. *e-mail: gchen@hit.edu.cn; ted.sargent@utoronto.ca

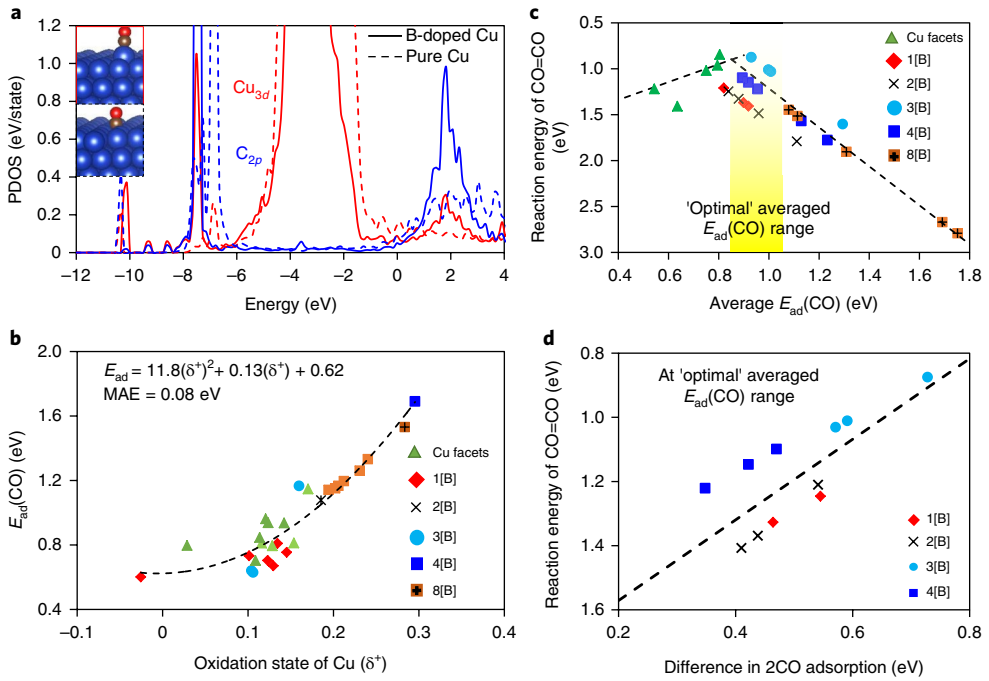

Fig. 1 | DFT calculations on enhancing C_2 electroproduction. a, PDOS plot of Cu_{3d} and C_{2p} orbitals in pure copper and boron-doped copper catalysts, suggesting CO has greater electronic interaction with copper in the Cu(B) system. **b**, The CO adsorption energy (E_{ad}) is monotonically increased as the partial positive oxidation state of copper is increased. MAE, mean absolute error. **c**, The CO=CO dimerization energy as a function of the average adsorption energy of two adsorbed CO molecules. This shows that an 'optimal' average adsorption energy of CO (~0.8–1.0 eV) can improve CO=CO dimerization during CO_2RR. **d**, When the 'optimal' average adsorption energy of CO is ~0.8–1.0 eV, a larger difference in the E_{ad} values of two CO molecules further enhances CO=CO dimerization. In **b**–**d**, 1[B], 2[B], 3[B], 4[B] and 8[B] refer to boron-doped copper catalysts with subsurface boron concentrations of 1/16, 1/8, 3/16, 1/4 and 1/2 monolayer, respectively.

charged copper oxidation state, indicating that the changes in the oxidation state of copper include the interaction between boron and copper, as well as the surface geometrical changes. Consequently, the boron-doped copper (Cu(B)) system has both $Cu^{\delta+}$ and Cu^0 regions, exhibiting a motif analogous to the Cu_2O/Cu catalyst reported by Goddard et al.[8].

We then simulated the Gibbs free energy of two key reaction pathways for a catalyst comprising boron-doped copper (1/16 monolayer) (Supplementary Fig. 10). We compared CO_2 reduction with C_1 (for example, methane) versus C_2 products (for example, C_2H_4 and C_2H_5OH) at 298 K and 1 atm. The boron dopant suppresses the reaction path of $CO_2 \rightarrow C_1$, increasing the reaction energy requirements for the (rate-limiting) $CO^* + H^* \rightarrow CHO^*$ step. Furthermore, it enhances $CO_2 \rightarrow C_2$ by decreasing the reaction energy required for the rate-limiting $CO^* + CO^* \rightarrow OCCO^*$ step.

We then proceeded to tune, still in computational studies, the partial copper oxidation state from −0.1 e to +0.3 e by varying the copper facets (that is, Cu(100), Cu(111), Cu(110) or Cu(211)), changing the concentration of boron dopants (from 1/16 monolayer to 1/2 monolayer, as shown in Supplementary Fig. 4 and Supplementary Table 1) and providing a range of applied external electric fields (Fig. 1b). The CO adsorption energy increases monotonically as the copper oxidation state is increased. A volcano plot of the energy for the CO=CO dimerization (the rate-limiting step for $CO_2 \rightarrow C_2$) as a function of the average CO adsorption energy ($E_{ad_{avg}} = \frac{E_{ad}(CO_{1st}) + E_{ad}(CO_{2nd})}{2}$) (Fig. 1c) indicates that—per the Sabatier principle—optimized average binding energies (~0.8–1.0 eV) of two CO molecules improve CO=CO dimerization and thus support the generation of C_2 products. When we applied a range of external electric fields and charged the surface[23–26] via the Neugebauer and Scheffler method[27], we found that the volcano plot of the CO=CO dimerization retains its profile and overall trends (Supplementary Fig. 11). Furthermore, when the optimal average binding energies of two CO molecules are achieved, a larger difference in the adsorption energies of these two CO molecules ($\Delta E_{ad} = |E_{ad}(CO_{1st}) - E_{ad}(CO_{2nd})|$) further enhances CO=CO dimerization (Fig. 1d). To increase C_2 production during the CO_2RR process, an optimal average oxidation state (~$\delta^{0.2+}$) for copper is desired and is driven by providing a local admixture of two different oxidation states of copper (δ^0 and δ^+). We find similar results on the (100) surface: boron-doped copper has a higher propensity to form C_2 products compared with pristine copper (see Supplementary Information). Taken together, these computational simulations point towards boron doping as a strategy to enhance C_2 production.

In light of these findings, we sought to synthesize boron-doped copper (Fig. 2a). The as-synthesized sample is of the cubic copper phase (Joint Committee on Powder Diffraction Standards (JCPDS) number 85-1326) with a dominant (111) peak (Supplementary Fig. 13). The Cu(B) sample has a porous dendritic morphology with nanostructured features on the scale of 30–40 nm (Supplementary Fig. 14). The presence of boron in Cu(B) samples was confirmed using X-ray photoelectron spectroscopy (XPS) (Fig. 2b and Supplementary Fig. 15). Other elements including sodium and chlorine were not detected before or after reaction (Supplementary Figs. 16 and 17), suggesting that only boron is incorporated into copper during the synthesis. The presence of boron in Cu(B) samples was further confirmed using inductively coupled plasma optical emission spectroscopy (ICP-OES) (Fig. 2c and Supplementary Fig. 18). We found the boron concentration inside the copper samples to be tunable when we varied the amount of the $CuCl_2$ precursor (Supplementary Table 8).

We sought to probe the distribution, as a function of depth within the copper-based catalyst, of the incorporated boron. We employed time-dependent ICP-OES (Fig. 2c), which revealed that the boron concentration drops from 5.7% (B/Cu atomic ratio) to

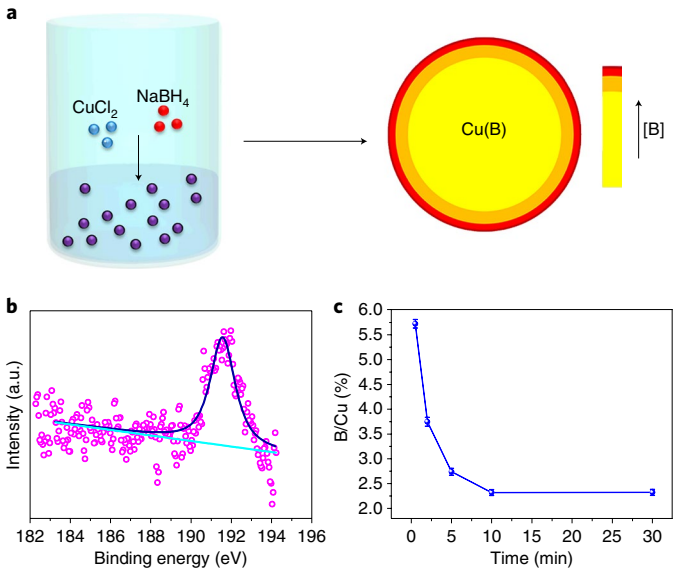

Fig. 2 | Preparation and characterization of Cu(B). a, Schematic of the wet-chemical process to synthesize Cu(B) samples. **b**,**c**, Boron XPS spectrum (magenta circle, raw data; blue line, fitted peak plot; cyan line, background) (**b**) and dissolving-time-dependent boron concentrations of the Cu(B) sample as measured by ICP-OES (**c**), indicating that boron is present on the surface of copper. The error bars represent the standard deviation of the results of three separate channels for each sample.

2.7% over an estimated depth of 7.5 nm. We found that the boron concentration is highest within 2.5 nm of the surface of the copper catalyst (Supplementary Fig. 19).

We used ultraviolet photoelectron spectroscopy to investigate the impact of boron doping on the electronic states of copper. We found that boron doping produces a shift in the valence band to a deeper level, in agreement with computational simulations (Supplementary Fig. 20). We then used X-ray absorption near-edge spectroscopy (XANES) to further investigate the impact of boron incorporation on the copper oxidation state. To exclude oxygen-containing species, we electrochemically reduced the Cu(B) samples by applying a highly negative potential (−0.5 to −2 V versus reversible hydrogen electrode (RHE), 0.1 V s^{-1}, 5 cycles). The absorption edges of all the Cu(B) samples reside between those of pristine copper (Cu^0) and Cu_2O (Cu^{1+}) (Fig. 3a and Supplementary Fig. 21). To give a direct comparison of the oxidation state of copper in the Cu(B) samples, we acquired the copper oxidation state as a function of copper K-edge energy shift (Fig. 3b). The average oxidation state of copper in the Cu(B) samples is found to vary from 0 to +1 as a function of the energy shift (Supplementary Table 9). The average oxidation state of copper increased from 0.25 to 0.78 as the boron concentration varied from 1.3 to 2.2%.

We investigated the oxidation state of samples under CO_2RR using in situ XANES. The oxidation state of copper increases with boron content under CO_2RR (Supplementary Fig. 22). To directly compare the copper oxidation state changes during the CO_2RR process, copper XANES spectra of Cu(B)-2 at different time points (immediately after cyclic voltammetry (CV) reduction, and 15 and 30 min later) relative to the onset of CO_2RR were recorded (Fig. 3c). We found the average oxidation state of copper in Cu(B)-2 during the in situ measurements to be +0.32, which is similar to the value obtained from the ex situ XANES results of Cu(B)-2 (0.35). These results indicate we observed a stable slightly positive oxidation state for copper in the Cu(B) samples over the course of CO_2RR (Supplementary Fig. 23).

Next, we sought to verify whether the copper oxidation state correlated with total C_2 Faradaic efficiency (Fig. 4a). When we

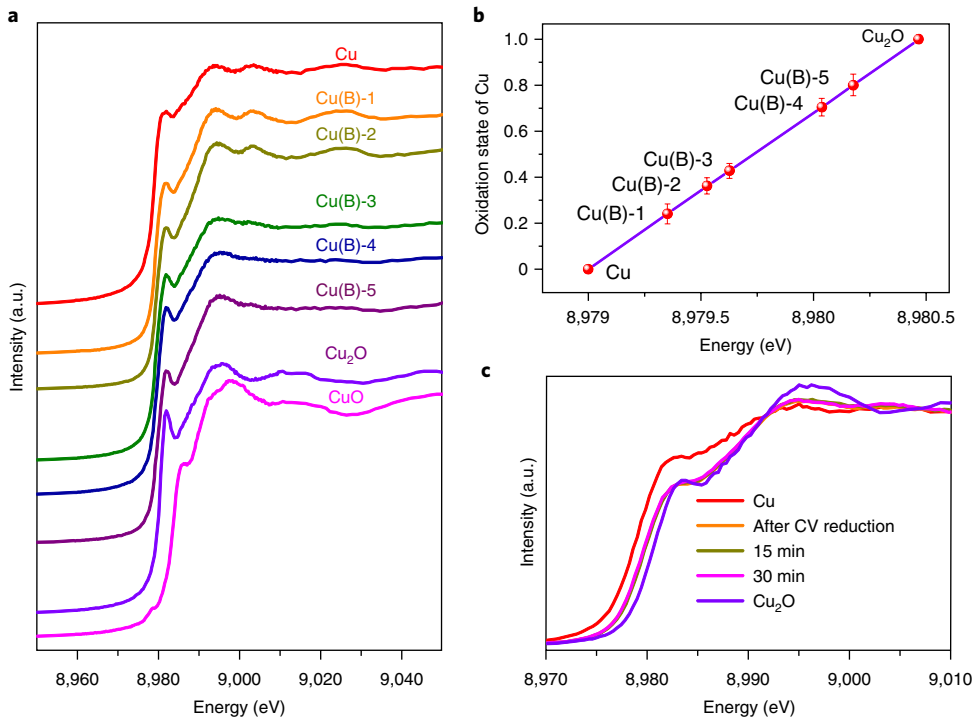

Fig. 3 | Oxidation state of copper in Cu(B) samples. a, Copper K-edge XANES spectra of Cu(B) samples after being electrochemically reduced. **b**, Average oxidation state of copper in Cu(B) with different contents of boron obtained from copper K-edge XANES, suggesting that the oxidation states of copper in Cu(B) samples are tunable. The error bars represent the standard deviation of three separate measurements for each sample. **c**, In situ copper K-edge XANES spectra of Cu(B)-2 immediately after CV reduction (orange), 15 min later (dark yellow) and 30 min later (magenta). Pristine copper (red) and Cu_2O (purple) are included as references. The edge position of each sample is determined from the intercept of the main edge and pre-edge contributions.

Table 1 | Summary of the current density and product distributions over Cu(B)-2 and control samples using 0.1 M KCl as an electrolyte under their respective optimal potentials

Sample	J (mA cm^{-2})[a]	Faradaic efficiency (%)[a]						
		H_2	CO	CH_4	C_2H_4	HCOOH	C_2H_5OH	C_3H_7OH
Cu(B)-2	70	20 ± 2	0	0.08	52 ± 2	0	27 ± 1	0
Cu(H)	51	44 ± 2	10 ± 1	8 ± 1	22 ± 1	6 ± 1	8 ± 1	2 ± 0.5
Cu(C)	70	66.4	8 ± 1	6 ± 1	33 ± 2	2 ± 0.5	14 ± 1	4 ± 0.5

[a]These values were obtained under the optimal potentials for C_2 of each sample (Cu(B)-2: −1.1 V versus RHE; Cu(H): −1.0 V versus RHE; Cu(C): −1.0 V versus RHE).

plotted the experimental C_2 Faradaic efficiency versus the experimental average copper oxidation state, we obtained a volcano plot that peaks with an impressive Faradaic efficiency of 79 ± 2% at an average copper valence of +0.35, showing agreement with our DFT predictions.

As controls, we also produced pristine copper (Cu(H)), which was synthesized following a previously reported procedure based on hydrazine hydrate[28]. We also produced reference catalysts that consisted of oxidized nano-copper (Cu(C)) (Supplementary Fig. 24). The Faradaic efficiencies for C_2 were 29 ± 2% for Cu(H) and 37 ± 2% for Cu(C) under their respective optimal potentials for C_2 electroproduction. The extreme selectivity of the boron-doped catalyst in favour of C_2 over C_1 is particularly striking: we achieved a maximum selectivity ratio of C_2:C_1 of 932 (Supplementary Table 10). Improved selectivity of C_2 over C_1 was further achieved on boron-doped Cu(111) single crystals (Supplementary Table 11) and in K_2HPO_4 electrolyte (Supplementary Table 12), indicating the generalizable concept that boron stabilizes the oxidation state of copper and drives electrochemical reduction of CO_2 to C_2 products.

The improved performance of the boron-doped catalyst is accompanied by a reduced onset potential for C_2 hydrocarbon electroproduction: −0.57 V (versus RHE) (Fig. 4c and Supplementary Fig. 25) for the best samples—0.1 V and 0.18 V lower than those of Cu(C) and Cu(H), respectively.

The presence of $Cu^{\delta+}$ sites on the copper surface is also predicted to increase the energy requirement for direct reduction of CO_2 to methane. For the Cu(B)-2 sample, the onset potential of methane is determined to be −1.1 V (versus RHE), which is 0.1 V higher than those of Cu(C) and Cu(H) (−1.0 V versus RHE). Interestingly, less than 0.5% of methane was detected during potentials ranging from −0.6 to −1.2 V (versus RHE). Moreover, only a slight increase of methane Faradaic efficiency (0.3%) was observed when we increased the potential by 0.1 V over and above the onset potential of methane. In contrast, the corresponding methane Faradaic efficiency increase was found to be ~2.0% for the Cu(C) and Cu(H) samples (Supplementary Fig. 25).

In summary, the direct reduction of CO_2 to methane is almost completely suppressed on the Cu(B)-2 sample. The onset potential of CO_2RR to C_2 hydrocarbons decreases to −0.57 V versus RHE while that for methane is substantially higher at −1.1 V versus RHE, showing a more favourable potential window for ethylene production.

The conversion efficiency of CO_2 to C_2 products increases dramatically as the applied voltage is rendered even more negative, towards −0.9 V versus RHE (Fig. 4b). The high C_2 selectivity is maintained over a wide potential window that spans −0.9 to −1.2 V versus RHE. The maximum Faradaic efficiency to ethylene (53 ± 1%) is achieved at −1.0 V versus RHE, which is 0.1 V lower than the onset potential for methane, accounting for the excellent selectivity of ethylene over methane in gas products (Supplementary Fig. 26).

Narrowing the product distribution is desired in the electrochemical CO_2RR process. The product distributions for the Cu(B)-2 sample versus the control samples were further investigated (Supplementary Fig. 27). Ethylene and ethanol are the major hydrocarbons from CO_2RR on Cu(B)-2, with a maximum Faradaic efficiency for C_2 products of 79 ± 2% and less than 0.1% of C_1 product (Table 1 and Supplementary Figs. 28 and 29) at −1.1 V versus RHE. Similar promoting effects that have the effect of narrowing the product distribution were also observed on other samples with different boron-doping concentrations (Supplementary Table 13). In contrast, in the case of the control samples, we obtained C_1 products with Faradaic efficiency of 24 ± 1% (Cu(H)) and 16% (Cu(C)) at their optimized applied potentials for the formation of C_2 products (Table 1). The ratios were $C_2/C_1 = 1.2$ for Cu(H) and $C_2/C_1 = 2.3$ for Cu(C). Formic acid and C_3 products were not detected on the Cu(B)-2 sample (Supplementary Figs. 30 and 31). Thus, the Cu(B) sample selectively generates C_2 products with a narrow product distribution.

Partial current density reports the activity of an electrocatalyst. A partial current density J_{C2} of 10 mA cm^{-2} is achieved for the case of the Cu(B)-2 sample when the applied potential is −0.74 V. This is much lower than the potentials to reach this same current for the cases of Cu(C) (−0.90 V versus RHE) and Cu(H) (−0.95 versus RHE).

We obtained a maximum J_{C2} (55 mA cm^{-2}) when operating the Cu(B)-2 sample at −1.1 V versus RHE. This is 3.7 and 1.7 times higher than the maximum J_{C2} for Cu(H) and Cu(C), respectively. We also report the current density normalized to the electrochemically active surface area (ECSA) (Supplementary Table 14 and Supplementary Figs. 32–34). Once the current is renormalized to the ECSA, the peak J_{C2} value is 3.0 and 1.9 times higher than those of the Cu(H) and Cu(C) cases.

We investigated charge transfer processes at the electrode/electrolyte interface using electrochemical impedance spectroscopy. Compared with Cu(H) and Cu(C), the diameter of the Nyquist circle for Cu(B)-2 is the smallest, indicating an acceleration in the charge transfer process between Cu(B)-2 and electrolyte (Supplementary Fig. 35). The improved charge transfer process reveals the low activation energy for the reactions on Cu(B)-2, which is further confirmed by linear sweep voltammetry and related Arrhenius plots (Supplementary Fig. 36). These results confirm the stability of the $Cu^{\delta+}$ sites and corroborate the Cu^0 and $Cu^{\delta+}$ favourability of the Cu(B) surface for the electroproduction of C_2 hydrocarbons.

Long-term stability remains a challenge for copper or modified copper despite their effectiveness in the electroreduction of CO_2 to multi-carbon hydrocarbons. We found that pristine copper (Cu(H)) shows only modest stability for CO_2RR to ethylene following 6 h of operation (Supplementary Fig. 37). Cu(C) shows slightly higher durability over this same time period (Fig. 4d).

The boron-doped copper showed superior stability, achieving 40 h of continuous operation at −1.1 V versus RHE (Supplementary Fig. 38) without loss of performance. This indicates that boron is stable as a dopant in copper (Supplementary Figs. 39–41). The $Cu^{\delta+}$ sites induced by boron doping are stable at high applied potential during the CO_2RR process (Fig. 3c), enabling its relative stability in performance.

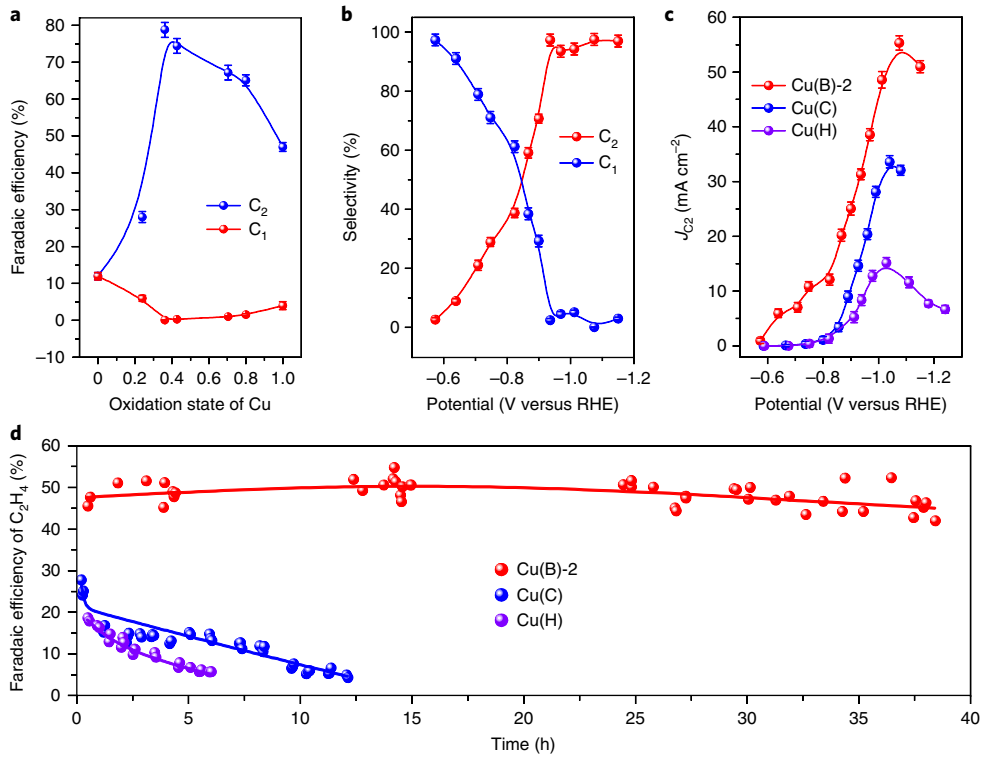

Fig. 4 | CO_2RR performance on Cu(B) and control samples. a, Faradaic efficiency of C_2 and C_1 at different copper oxidation states on Cu(B). All samples were tested using the same potential of -1.1 V versus RHE. **b**, Conversion efficiency of reacted CO_2 to C_2 and C_1 products at different potentials on Cu(B)-2. **c**, Partial current density of C_2 at different potentials on Cu(B)-2, Cu(C) and Cu(H). **d**, Faradaic efficiency of ethylene on Cu(B)-2, Cu(C) and Cu(H). The boron-doped copper catalyst showed the highest selectivity, conversion efficiency and partial current density of C_2 hydrocarbons. Error bars represent the standard deviation of three separate measurements for an electrode.

Conclusion

In summary, highly selective C_2 products from CO_2RR were obtained on boron-doped copper with stable electron localization. The electroreduction of CO_2 to C_2 hydrocarbons, and its link with the oxidation state of copper, were theoretically and experimentally confirmed. At the average copper valence state of +0.35, a high Faradaic efficiency for C_2 hydrocarbons of ~80% was achieved. Under these conditions, C_1 products are completely suppressed in both gas and liquid products. Boron-doped copper showed superior stability for CO_2RR to C_2, achieving ~40 h of initial sustained efficient operation.

Methods

DFT calculations. DFT calculations were performed using Vienna Ab initio Simulation Package code[29,30]. Full computational simulation details are provided in the Supplementary Information.

Preparation of catalyst samples. Cu(B) samples were prepared through a facile one-step process using copper(II) chloride ($CuCl_2$) and sodium borohydride ($NaBH_4$) as precursors. Since boron solubility in copper is low, $CuCl_2$ was added into highly concentrated sodium borohydride solution instantly in order to alloy the boron with copper at as high loading as possible[31,32]. First, $CuCl_2$ and $NaBH_4$ were prepared using frozen water (~0 °C). Next, 2 ml $CuCl_2$ solution with a certain concentration was injected rapidly into the $NaBH_4$ (5 M, 2 ml) solution until no bubbles formed. The precipitates obtained were subsequently washed three times with 150 ml of water (50 ml each time) and once with 50 ml of acetone to completely remove the unreacted precursors and other possible byproducts. Then, the powder was immediately dried under vacuum overnight. Different amounts of $CuCl_2$ (namely, 400 mg for Cu(B)-1, 300 mg for Cu(B)-2, 200 mg for Cu(B)-3, 100 mg for Cu(B)-4 and 25 mg for Cu(B)-5) were used. The control sample Cu(H) was synthesized following a similar procedure but using an equal amount of hydrazine hydrate instead of $NaBH_4$ as the reducing reagent. Some 25 nm partially oxidized nano-copper (Sigma) was also used as a control sample in this work.

The boron-doped Cu(111) surface sample was synthesized by incipient wetness impregnation of single-crystal Cu(111) foil with boric acid aqueous solutions. After impregnation, the copper foil was dried and then calcinated at 500 °C in H_2/Ar gas (5 vol.% H_2) for 6 h. The presence of boron was confirmed by XPS testing (Supplementary Fig. 42).

ECSA measurement. All electrodes were electrochemically reduced using the CV method (−0.5 V to −2 versus RHE, 0.1 V s^{-1}, 5 cycles) before ECSA measurements. The lead under-potential deposition method was used to estimate the ECSA of boron-doped copper and control samples. Briefly, a freshly prepared 50 ml solution containing 100 mM of $HClO_4$ with 0.5 mM of $PbCl_2$ and 50 mM KCl was used. Next, the electrode was held at −0.375 V for 10 min before the stripping of lead by sweeping the potential from −0.5 to −0.1 V (versus Ag/AgCl) at 10 mV s^{-1}. The copper ECSA calculations assume a monolayer of lead adatom coverage over copper and $2e^-$ lead oxidation with a conversion factor of 310 μC cm^{-2}.

The ECSA values of the as-made electrodes were also evaluated by CV using the ferri-/ferrocyanide redox couple ($[Fe(CN)_6]^{3-/4-}$) as a probe. Cyclic voltammetry was carried out in a nitrogen-purged 5 mM $K_3Fe(CN)_6$/0.1 M KCl solution with platinum gauze as the counter electrode. ECSA values were calculated using the Randles–Sevcik equation:[9]

$$I_p = (2.36 \times 10^5) n^{3/2} A D^{1/2} C \nu^{1/2}$$

I_p is peak current (A), $n = 1$, $D = 4.34 \times 10^{-6}$ cm^2 s^{-1}, A is the electrochemical active surface area (cm^2), C is the concentration of potassium ferricyanide (5×10^{-6} mol cm^{-3}) and ν is the scan rate (5 mV s^{-1}).

Characterization. The crystal structures of the samples were characterized with a powder X-ray diffractometer (MiniFlex600) using Cu Kα radiation (λ = 0.15406 nm). A scanning electron microscope (Hitachi SU8230) and electron tomography in a transition electron microscope (TEM) (FEI Tecnai G^2) were employed to observe the morphology of the samples. A tilt series of two-dimensional TEM images for electron tomography was acquired from −75 to +75° with a tilt increment of 3° at 200 kV. The series was used as an input for three-dimensional reconstruction using the SIRT algorithm implemented in the ASTRA toolbox[33]. XPS measurements were carried out on a K-Alpha XPS spectrometer (PHI 5700 ESCA System) using Al Kα X-ray radiation (1,486.6 eV)

for excitation. The line of carbon C1*s* with the position at 284.6 eV was used as a reference to correct the charging effect. Ultraviolet photoelectron spectroscopy spectra were measured using He I excitation (21.2 eV) with a SPECS PHOIBOS 150 hemispherical energy analyser in the ultrahigh vacuum chamber of the XPS instrument. Angle-dependent XPS measurements were also carried out using this same XPS instrument. ICP-OES (Optima 7300 DV) was carried out to determine the boron contents doped into copper. In total, 1 mg of the samples was completely dissolved into 50 ml trace metal HNO_3 (5 mM) using a sonication bath for 30 min for the ICP-OES test. Dissolving-time-dependent ICP-OES experiments were carried out by withdrawing 10 ml of the solution at time 0 (~10 s), 2 min, 5 min, 10 min and 30 min. Ex situ X-ray absorption measurements at the copper K-edges were performed at the 20-BM-B beamline at the Advanced Photon Source (APS) at Argonne National Laboratory. In situ X-ray absorption spectroscopy (XAS) measurements at the copper K-edges were performed at the Soft X-ray Microcharacterization Beamline 06B1-1 at Canadian Light Source (CLS).

Preparation of cathode electrodes. The catalyst ink was prepared by ultrasonic dispersion of 10 mg of the sample powder with 20 µl Nafion solution (5%) in 1 ml methanol for 30 min. Next, 5 µl of the as-prepared ink was drop-coated on the glass carbon electrode with a surface area of 0.07 cm^2. The electrode was then dried under methanol atmosphere slowly for the subsequent electrochemical testing experiments.

Catalytic evaluation. All CO_2 reduction experiments were performed in a gas-tight two-compartment H-cell separated by an ion exchange membrane (Nafion117). The anode and cathode sides were filled with 55 ml of 0.1 M $KHCO_3$ and 0.1 M KCl, respectively. The reaction was performed at constant iR-corrected potential. First, the cathode side was electrochemically reduced using the CV method, which ranged from −0.5 to −2.0 V (versus RHE) at a rate of 0.1 V s^{-1} for 5 cycles to completely reduce the possible oxidized species. The gas products from CO_2 reduction were analysed using the gas chromatograph (PerkinElmer Clarus 600) equipped with thermal conductivity and flame ionization detectors. The liquid samples were collected and analysed by NMR instruments by taking (Agilent DD2 500) dimethylsulfoxide as a reference. The potential (versus Ag/AgCl) was converted to RHE using the following equations:

$$E_{RHE} = E_{AgCl} + 0.059\ pH + E^0_{AgCl}$$

$$E^0_{AgCl}\ (3.0\ M\ KCl) = 0.209\ V (25\ ^\circ C)$$

Data availability. The data supporting the findings of this study are available within the article and its Supplementary Information files. All other relevant source data are available from the corresponding author upon request.

Received: 2 October 2017; Accepted: 29 May 2018;
Published online: 16 July 2018

References

1. Farrell, A. E. et al. Ethanol can contribute to energy and environmental goals. *Science* **311**, 506–508 (2006).
2. Hill, J., Nelson, E., Tilman, D., Polasky, S. & Tiffany, D. Environmental, economic, and energetic costs and benefits of biodiesel and ethanol biofuels. *Proc. Natl Acad. Sci. USA* **103**, 11206–11210 (2006).
3. Bushuyev, O. S. et al. What should we make with CO_2 and how can we make it?. *Joule* **5**, 825–832 (2017).
4. Loiudice, et al. Tailoring copper nanocrystals towards C_2 products in electrochemical CO_2 reduction. *Angew. Chem. Int. Ed.* **55**, 5789–5792 (2016).
5. Mistry, H. et al. Highly selective plasma-activated copper catalysts for carbon dioxide reduction to ethylene. *Nat. Commun.* **7**, 12123 (2016).
6. Yano, H., Tanaka, T., Nakayama, M. & Ogura, K. Selective electrochemical reduction of CO_2 to ethylene at a three-phase interface on copper(I) halide-confined Cu-mesh electrodes in acidic solutions of potassium halides. *J. Electroanal. Chem.* **565**, 287–293 (2004).
7. Kuhl, K. P., Cave, E. R., Abram, D. N. & Jaramillo, T. F. New insights into the electrochemical reduction of carbon dioxide on metallic copper surfaces. *Energy Environ. Sci.* **5**, 7050 (2012).
8. Xiao, H., Goddard, W. A. 3rd, Cheng, T. & Liu, Y. Cu metal embedded in oxidized matrix catalyst to promote CO_2 activation and CO dimerization for electrochemical reduction of CO_2. *Proc. Natl Acad. Sci. USA* **114**, 6685–6688 (2017).
9. Allen, J. & Bard, L. R. F. *Electrochemical Methods: Fundamentals and Applications* (Wiley, New York, NY, 2000).
10. De Luna, P. et al. Catalyst electro-redeposition controls morphology and oxidation state for selective carbon dioxide reduction. *Nat. Catal.* **1**, 103–110 (2018).
11. Ren, D. et al. Selective electrochemical reduction of carbon dioxide to ethylene and ethanol on copper(I) oxide catalysts. *ACS Catal.* **5**, 2814–2821 (2015).
12. Lee, S. & Lee, J. Electrode build-up of reducible metal composites toward achievable electrochemical conversion of carbon dioxide. *ChemSusChem* **9**, 333–344 (2016).
13. Eilert, A., Roberts, F. S., Friebel, D. & Nilsson, A. Formation of copper catalysts for CO_2 reduction with high ethylene/methane product ratio investigated with in situ X-ray absorption spectroscopy. *J. Phys. Chem. Lett.* **7**, 1466–1470 (2016).
14. Li, C. W. & Kanan, M. W. CO_2 reduction at low overpotential on Cu electrodes resulting from the reduction of thick Cu_2O films. *J. Am. Chem. Soc.* **134**, 7231–7234 (2012).
15. Roberts, F. S., Kuhl, K. P. & Nilsson, A. High selectivity for ethylene from carbon dioxide reduction over copper nanocube electrocatalysts. *Angew. Chem. Int. Ed.* **127**, 5268–5271 (2015).
16. Gao, D. et al. Plasma-activated copper nanocube catalysts for efficient carbon dioxide electroreduction to hydrocarbons and alcohols. *ACS Nano* **11**, 4825–4831 (2017).
17. Favaro, M. et al. Subsurface oxide plays a critical role in CO_2 activation by Cu(111) surfaces to form chemisorbed CO_2, the first step in reduction of CO_2. *Proc. Natl Acad. Sci. USA* **114**, 6706–6711 (2017).
18. Lee, S., Kim, D. & Lee, J. Electrocatalytic production of C_3-C_4 compounds by conversion of CO_2 on a chloride-induced bi-phasic Cu_2O–Cu catalyst. *Angew. Chem. Int. Ed.* **54**, 14701–14705 (2015).
19. Larrazabal, G. O., Martin, A. J., Krumeich, F., Hauert, R. & Perez-Ramirez, J. Solvothermally-prepared Cu_2O electrocatalysts for CO_2 reduction with tunable selectivity by the introduction of p-block elements. *ChemSusChem* **10**, 1255–1265 (2017).
20. Grace, A. N. et al. Electrochemical reduction of carbon dioxide at low overpotential on a polyaniline/Cu_2O nanocomposite based electrode. *Appl. Energy* **120**, 85–94, (2014).
21. Trinh, Q. T., Banerjee, A., Yang, Y. H. & Mushrif, S. H. Sub-surface boron-doped copper for methane activation and coupling: first-principles investigation of the structure, activity, and selectivity of the catalyst. *J. Phys. Chem. C* **121**, 1099–1112 (2017).
22. Soon, A., Todorova, M., Delley, B., & Stampfl, C. Oxygen adsorption and stability of surface oxides on Cu(111): a first-principles investigation. *Phys. Rev. B* **73**, 165424 (2006).
23. Goodpaster, J. D., Bell, A. T. & Head-Gordon, M. Identification of possible pathways for C–C bond formation during electrochemical reduction of CO_2: new theoretical insights from an improved electrochemical model. *J. Phys. Chem. Lett.* **7**, 1471–1477 (2016).
24. Montoya, J. H., Peterson, A. A. & Nørskov, J. K. Insights into C–C coupling in CO_2 electroreduction on copper electrodes. *ChemCatChem* **5**, 737–742 (2013).
25. Cheng, T., Xiao, H. & Goddard, W. A. III Free-energy barriers and reaction mechanisms for the electrochemical reduction of CO on the Cu(100) surface, including multiple layers of explicit solvent at pH 0. *J. Phys. Chem. Lett.* **6**, 4767–4773 (2015).
26. Filhol, J. S. & Neurock, M. Elucidation of the electrochemical activation of water over Pd by first principles. *Angew. Chem. Int. Ed.* **45**, 402–406 (2006).
27. Neugebauer, J. & Scheffler, M. Adsorbate–substrate and adsorbate–adsorbate interactions of Na and K adlayers on Al(111). *Phys. Rev. B* **46**, 16067–16080 (1992).
28. Gawande, M. B. et al. Cu and Cu-based nanoparticles: synthesis and applications in catalysis. *Chem. Rev.* **116**, 3722–3811 (2016).
29. Kresse, G. & Hafner, J. Ab initio molecular dynamics for liquid metals. *Phys. Rev. B* **47**, 558–561 (1993).
30. Kresse, G. & Furthmüller, J. Efficiency of ab-initio total energy calculations for metals and semiconductors using a plane-wave basis set. *Comput. Mat. Sci.* **6**, 15–50 (1996).
31. Massalski, T. B., Okamoto, H., Subramanian, P. R. & Kacprzak, L. *Binary Alloy Phase Diagrams* 2nd edn (ASM International, OH, 1990).
32. Carenco, S., Portehault, D., Boissiere, C., Mezailles, N. & Sanchez, C. Nanoscaled metal borides and phosphides: recent developments and perspectives. *Chem. Rev.* **113**, 7981–8065 (2013).
33. Van Aarle, W. et al. The ASTRA Toolbox: a platform for advanced algorithm development in electron tomography. *Ultramicroscopy* **157**, 35–47 (2015).

Acknowledgements

This work was supported financially by funding from TOTAL S.A., the Ontario Research Fund: Research Excellence Program, the Natural Sciences and Engineering Research Council of Canada, the CIFAR Bio-Inspired Solar Energy programme, a University of Toronto Connaught grant, the Ministry of Science, Natural Science Foundation of China (21471040, 21271055 and 21501035), the Innovation-Driven Plan in Central South University project (2017CX003), a project from State Key Laboratory of Powder Metallurgy in Central South University, the Thousand Youth Talents Plan of China and Hundred Youth Talents Program of Hunan and the China Scholarship Council programme. This work benefited from the soft X-ray microcharacterization beamline at CLS, sector 20BM at the APS and the Ontario Centre for the Characterisation of Advanced Materials at the University of Toronto. H.Y. acknowledges financial support from the

Research Foundation-Flanders (FWO postdoctoral fellowship). C.Z. acknowledges support from the International Academic Exchange Fund for Joint PhD Students from Tianjin University. P.D.L. acknowledges financial support from the Natural Sciences and Engineering Research Council in the form of the Canada Graduate Scholarship—Doctoral award. S.B. and E.B. acknowledge financial support from the European Research Council (ERC Starting Grant #335078-COLOURATOMS). The authors thank B. Zhang, N. Wang, C. T. Dinh, T. Zhuang, J. Li and Y. Zhao for fruitful discussions, as well as Y. Hu and Q. Xiao from CLS, and Z. Finfrock and M. Ward from APS for their help during the course of study. Computations were performed on the SOSCIP Consortium's Blue Gene/Q computing platform. SOSCIP is funded by the Federal Economic Development Agency of Southern Ontario, the Province of Ontario, IBM Canada, Ontario Centres of Excellence, Mitacs and 15 Ontario academic member institutions.

Author contributions

E.H.S. and G.C. supervised the project. Y.Z. and M.L. conceived the idea, designed the experiments and analysed the results. Y.Z. synthesized the samples, performed the electrochemical experiments and analysed the results. F.C. carried out the simulations and wrote the corresponding section. M.L., P.C. and P.D.L. conducted the XAS measurements. J.L., Z.W., T.-K.S. and D.S. assisted in analysing the XAS results. C.Z., Y.Z. and Z.L. ran the NMR tests. M.L. and C.Z. carried out the scanning electron microscope measurements. Y.Z. and H.Y. designed the ICP-OES experiments. C.Z. performed the ICP-OES tests. Z.L. ran the X-ray diffractometer tests. R.Q.-B., H.X. and H.L. performed the XPS measurements. E.B. conducted the TEM measurements. E.B., H.Y., S.B. and J.H. assisted in analysing the TEM results. All authors read and commented on the manuscript.

Competing interests

The authors declare no competing interests.

Additional information

Supplementary information is available for this paper at https://doi.org/10.1038/s41557-018-0092-x.

Reprints and permissions information is available at www.nature.com/reprints.

Correspondence and requests for materials should be addressed to G.C. or E.H.S.

Publisher's note: Springer Nature remains neutral with regard to jurisdictional claims in published maps and institutional affiliations.